

DMSP Space Wx  
SSJ, SSIES, SSM Instrument  
Data Processing  
to  
Community Products “User’s Guide”

Revision 1.0, January 15, 2015



Artistic representation of a DMSP Block-5D2 spacecraft (source: <http://www.af.mil/>).

**Prepared By:** Robert J. Redmon

**Contributors:** D. Ober, F. Rich, J.V. Rodriguez, D. Knipp, L. Kilcommons

## Summary

This is a Public User's Guide. The purpose of this document is to spell out the specifics of the project to create DMSP space weather particles and fields data products in standardized formats that are readily consumable by space weather researchers and their commonly used tools (e.g. CDAWeb). Support has been provided by NOAA/NGDC and NASA grant #NNX13AG07G (PI D. Knipp). This document is a dynamic publicly accessible and authoritative user's guide for the DMSP SSJ, SSIES and SSM data available from the NGDC archive. This User's Guide is a central resource including new information and references to existing documentation offered by AFRL and other contributing institutes (e.g. UTD for SSIES, JHU/APL for SSJ).

This is a fluid, working document. All authors and readers are encouraged to provide comments and criticisms as they arise.

## Document Revision History

Date	Description	Preparer	Version
01/15/2015	First version disseminated.	R.J. Redmon	1.0

## Table of Contents

[Summary](#)

[Document Revision History](#)

[Table of Contents](#)

[1 Introduction](#)

[2 Scientific Products, Uncertainties and Quality Flags](#)

[2.1 Ephemeris](#)

[2.1.1 Auroral Boundaries](#)

[2.1.2 Ephemeris Validation](#)

[2.1.3 Caveats and Known Bugs](#)

[2.1.4 Revision History](#)

[2.2 SSJ Precipitating Electrons and Ions](#)

[2.2.1 SSJ Validation](#)

[2.2.2 Caveats and Known Bugs](#)

[2.2.3 Revision History](#)

[2.3 SSM Magnetic Field and Perturbations](#)

[2.3.1 SSM Validation](#)

[2.3.2 Uncertainty in the SSM measurements](#)

[2.3.3 Caveats and Known Bugs](#)

[2.3.4 Revision History](#)

[2.4 SSIES Bulk Plasma Parameters](#)

[2.4.1 SSIES Validation](#)

[2.4.2 Caveats and Known Bugs](#)

[2.4.3 Revision History](#)

[5 Public Data Access and Tools](#)

[6 References](#)

[7 Appendices](#)

[7.1 Ephemeris](#)

[7.2 SSJ Detector Efficiencies](#)

[7.3 Velocity Direction Approximation](#)

[7.3 Acronyms](#)

# 1 Introduction

TBD: Add spacecraft image showing instruments and their orientation w.r.t. s/c direction.

Figure 1 illustrates the value of observing a comprehensive set of plasma parameters from the same spaceborne platform, including precipitating electrons and ions, the vector magnetic field, and bulk ion density and vector velocity as measured by the F13 spacecraft during a northern auroral crossing in 1998.

**Example stack plot from SSDP showing common parameters for F13 in 1998:**

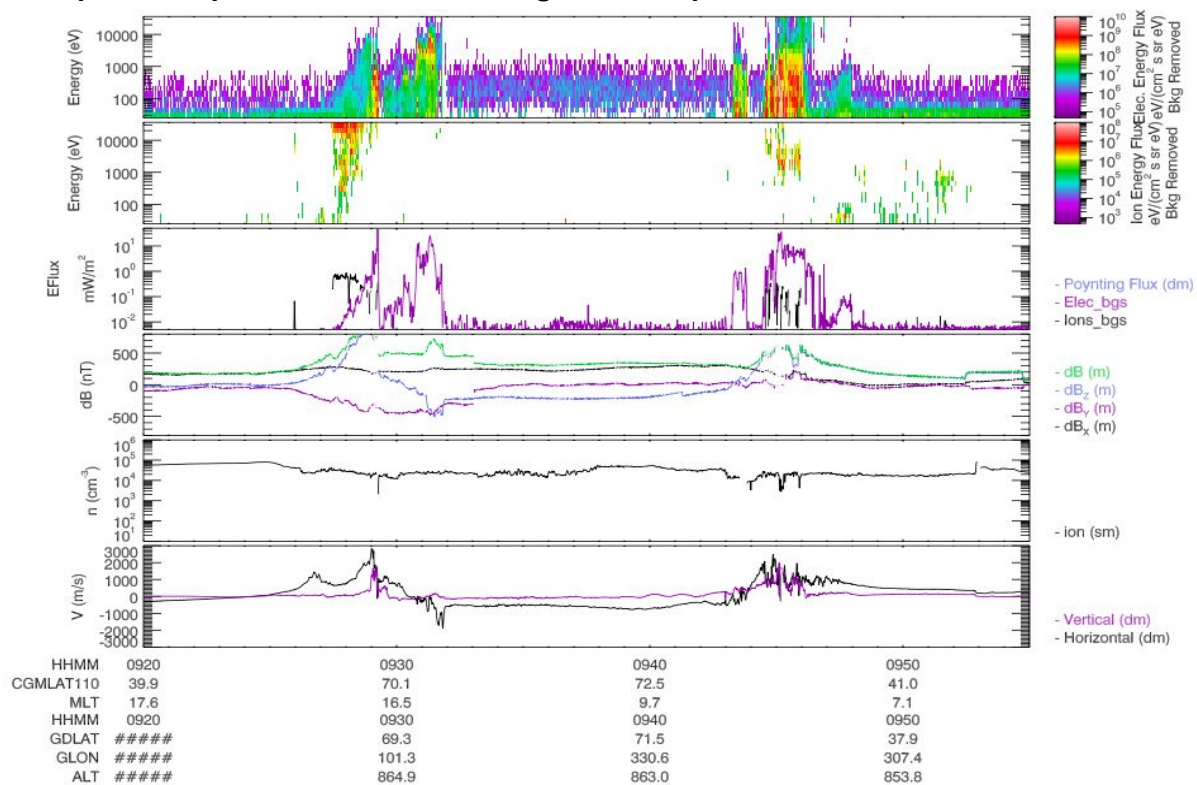


Figure 1: Time series stack plot using the SSDP application. From top to bottom: a) electron and b) ion differential energy flux (background subtracted) from the SSJ, c) total energy flux for electrons (purple), ions (black) from the SSJ, d) magnetic field deviations from the model given as total (green), and the x- (black), y- (purple) and z- (blue) component directions from the SSM; e) ion density ( $\text{cm}^{-3}$ ) from the Scintillation Meter (SM), f) bulk velocities from the Ion Drift Meter (IDM) in the spacecraft horizontal (black) and vertical (purple) directions. [TBD: Update x-labels, remove #'s.]

## 2 Scientific Products, Uncertainties and Quality Flags

Beyond providing quality ephemerides and other contextual information, the final output contains several important scientifically useful products. Alongside these products, known and

propagated uncertainties are also be given.

## 2.1 Ephemeris

TBD:

- AACGM IDL version used and epoch interpolation
- Backup: Sattrack, SGP4, Celestrak, Kelso, Vallado...
- Correction to doc at Wisconsin eci2geo (and remaining confusion...)

The spacecraft ephemeris is provided in several coordinate frames and on the same cadence and precise timestamps of the measurements (e.g. 1-second for SSJ). The coordinate frames provided are Earth Centered Inertial (ECI) True of Date (TOD) Epoch, Geocentric (GEO), and Altitude Adjusted Corrected Geo Magnetic (AACGM). Here we describe the processing details arriving at these ephemeris coordinate frames. The expected accuracy in the ECI and GEO frames is on the order of a few kilometers.

The DMSP spacecraft estimate their location on board, and telemetry ground processing bundles these 1-minute estimates within instrumental data files which are ultimately conveyed to NGDC via Boston College as day files. These estimated ephemerides are sufficient for operational purposes but are generally in significant disagreement with ephemerides computed in retrospect such as by the North American Aerospace Defense Command (NORAD) and the disagreement should be worse for flight models without on board Global Positioning System (GPS) systems (e.g. F14 and earlier). Interpretation of the vector magnetic measurements is the most sensitive of the environmental measurements to spacecraft location inaccuracies (e.g. Alken et al., 2014; Knipp et al., 2014).

We developed two tools to compute more accurate ephemerides, one based on propagating Two Line Elements (TLE) using the Simplified General Perturbations (SGP) theory (TBD: REF: Vallado et al.; Kelso et al.) and the other based on interpolating ECI(TOD) estimates from the NASA Space Physics Data Facility (SPDF). While, for specific applications, data users may request ephemeris estimates from NGDC using the SGP approach, our standard processing uses the latter approach which we will now describe in greater detail. Two common systems used in practice to specify a coordinate in the ECI frame include the True of Date (TOD) and the “mean equator and equinox of 2000” (J2000) (Tapley et al., 2004, pp. 31, 74). The TOD system identifies the true equator and equinox for the date of the specified coordinate, while the J2000 system is fixed to the date January 1, 2000, 12:00UT. Thus the TOD equinox is time-varying in space while the J2000 equinox is fixed. We use the TOD system herein labeled as  $ECI_{TOD}$ . We gather 1-minute  $ECI_{TOD}$  estimates from the SPDF’s Spacecraft Locator tool (<http://sscweb.gsfc.nasa.gov/cgi-bin/Locator.cgi>), and use an 8th order interpolation ([Appendix 7.1](#)) (Burden et al., 1993; Minter 2002) to arrive at the spacecraft location in  $ECI_{TOD}$  on the timestamps of environmental measurements. A one day comparison between 1-second  $ECI_{TOD}$  and 1-minute  $ECI_{TOD}$  interpolated onto the second (86,400 points) yielded a Root Mean Squared

Error (RMSE) less than 6 meters per axis, showing this interpolation scheme to be numerically sufficient.

The IDL Astronomy User's Library (IDL Astro) "eci2geo" routine is then used to rotate our  $\text{ECI}_{\text{TOD}}$  locations to the Geocentric (GEO) frame. The IDL Astro repository and "eci2geo" routine are located at:

<http://idlastro.gsfc.nasa.gov/>

<http://idlastro.gsfc.nasa.gov/ftp/pro/astro/eci2geo.pro>

Testing of the "eci2geo" routine revealed that it's transformation is most consistent with expecting ECI in the TOD system as it's input and the IDL Astro documentation has been corrected accordingly (private communication P. Saint Hilaire, 2014). We use the Super Dual Auroral Radar Network (SuperDARN) IDL AACGM library (TBD: Ref. R. Barnes; Code Version #; magnetic coefficients through 2010) to transform GEO to AACGM latitude, longitude and Magnetic Local Time (MLT). It's important to ensure various calculators are using the same geocentric radius or to adjust accordingly. IDL Astro "eci2geo" uses a radius of 6378.137 (Earth approximate equatorial radius) while AACGM uses 6371.2 (Earth mean radius). So, we make the minor adjustment before rotating GEO to AACGM. Since AACGM does not use time varying magnetic field coefficients, we approximate the time dependence by linearly interpolating the two AACGM latitude, longitude and MLT estimates computed at the two nearest 5-year epochs onto the instrument timestamp. This is a minor adjustment. Since the latest AACGM magnetic coefficients currently available are from 2010, dates after 2010 are not interpolated.

Modified Apex (henceforth called simply Apex) coordinates (Richmond, 1995) are also included in the case of the CDF files for the magnetometer (SSM). The Apex coordinate system is also 'altitude adjusted' similar to AACGM, with the additional feature of allowing the user to choose which altitude field lines will be traced to. Whereas the AACGM system always is referenced to the ground (0 km altitude), we have chosen the reference altitude for Apex to be 110 kilometers, roughly the ionosphere. This choice is the software default, and is commonly used as it is the expected reference when magnetometer measurements are ingested by the Assimilative Mapping of Ionospheric Electrodynamics (AMIE) procedure. Modified Apex is a generalized curvilinear coordinate system, and can only be completely described by two sets of basis vectors,  $\{e_1, e_2, e_3\}$  and  $\{d_1, d_2, d_3\}$ . We suggest that users interested in estimating field aligned currents using these data ensure they have a full understanding of the implications of these covariant/contravariant bases to avoid silly mathematical errors.

The Apex SSM vector magnetic perturbations are supplied in the 'd' basis, in which

$d_1$  points along a local contour of increasing apex longitude

$d_2$  is parallel to a local contour of decreasing absolute apex latitude (equatorward)

$d_3$  is parallel to the local geomagnetic (IGRF) field vector

The IGRF coefficients used for the Apex mapping are interpolated to the nearest year. Dates after 2010 are not interpolated.

The ephemeris parameters offered in the public CDF repository are:

Quantity	Units	Description	Dimensionality
SC_ECI	km	Earth Centered Inertial (TOD)	3
SC_GEOCENTRIC_LAT	degrees	Geocentric Latitude	1
SC_GEOCENTRIC_LON	degrees	Geocentric Longitude	1
SC_GEOCENTRIC_R	km	Geocentric Radius	1
SC_AACGM_LAT	degrees	AACGM Latitude	1
SC_AACGM_LON	degrees	AACGM Longitude	1
SC_AACGM_LTIME	hours	AACGM Local Time	1

### 2.1.1 Auroral Boundaries

To facilitate scientific studies of auroral phenomena, we have used data from the SSJ instrument to include auroral boundary locations with each CDF file. The 'AURORAL\_REGION' CDF variable contains an integer code indicating the region the spacecraft was passing through at the record's timestamp. The levels are:

- (0) No boundary identified for this pass
- (1) Below the auroral oval
- (2) In the auroral region
- (3) In the polar region

Also included is an 'ORBIT\_INDEX' CDF variable, which is an integer code which indicates the orbit number since the start of the day. The index increments once every complete orbit, but points in the southern hemisphere are assigned -1 times the index. This allows the analyst to easily subdivide a particular orbit into it's hemispheres, or, for example select only northern hemisphere passes. The start of each orbit is determined as the first record after the Apex magnetic equator. An index of 0 is assigned to points before the first equator crossing of the day.

Our auroral boundary finding algorithm is a Python reimplementaion of the Redmon boundary finding IDL routines (Redmon et al., 2010; Redmon 2012). The algorithm works by, for each polar region crossing (half-orbit), first detecting regions of high energy (30keV to 1.39keV) integrated electron energy flux continuously above a certain threshold ( $10^{8.5}$  eV/cm<sup>2</sup>/s/sr for the current version of the dataset), and then inter-comparing them to determine which two are most likely to represent the ascending and descending crossings of the auroral oval.

Choosing which two above-threshold segments are most likely to be the actual auroral crossings involves maximizing the following figure-of-merit (FOM):

$$\begin{aligned}
 FOM(seg\_1, seg\_2) = & (A_1 + A_2)/A_{Max} \\
 & + (1 - \overline{\sigma_{A1}}/A_1) + (1 - \overline{\sigma_{A2}}/A_2) \\
 & + polar\_region\_time\_width/(20.*60.)
 \end{aligned}$$



where the subscript 1 corresponds to ascending and subscript 2 represents descending side of the maximum latitude of the auroral oval crossing,  $\overline{A}$  represents the sum of the integrated >1keV electron energy flux over this auroral crossing,  $\sigma_A/\overline{A}$  represents the mean relative uncertainty in the integrated flux for the auroral crossing ( the uncertainty terms penalize regions of low background-adjusted precipitation ) and the last term quantifies the width of the polar region (in terms of the time the spacecraft spent crossing it) as a fraction of the average time the spacecraft spends crossing the high latitudes (20 minutes).  $A_{Max}$  is different for every half-orbit, and indicates the  $A$  value of the crossing candidate region with the maximum total flux.

Note that, while related, this FOM and the FOM used in Redmon, 2010 are different. Because of the addition of relative uncertainty to the SSJ dataset, we were able to add that information to the FOM and improve boundary detection. Values of this new FOM range from 0 to around 4, with higher values still indicating more optimal crossings.

While the FOM provides a measure of the believability of the boundary identification, we have chosen to discard particularly untrustworthy identifications, including all passes which intersect the oval, but do not cross into the polar region. Such data will have 'AURORAL\_REGION' CDF variable values of 0. Also, we encourage cautious interpretation of boundaries which intersect the dayside cusp and surrounding regions. It has been noted that intermittent high energy precipitation often continues poleward of the true boundary in these passes, and the algorithm will occasionally misidentify the poleward edge on the dayside. While we have endeavoured to tune the algorithm to avoid such misidentifications, we can not guarantee their absence.

We also compute an auroral boundary “latitude”, as in Redmon, 2010 which is simply a measure of distance from the spacecraft location to the auroral boundary. It is especially useful for organizing observations from many orbits as a function of boundary location (removes the effect of the expanding and contracting auroral oval, creating a dynamic boundary coordinate system). This quantity is defined piecewise with three parts:

$$\begin{aligned} L_{eq} &= (|mlat\_azb| - |mlat(t)|)/(|mlat\_azb|) \text{ [equatorward of the auroral zone]} \\ L_{az} &= (|mlat(t)| - |mlat\_azb|)/(|mlat\_pcb| - |mlat\_azb|) \text{ [in the auroral zone]} \\ L_{pc} &= (|mlat(t)| - |mlat\_pcb|)/(90 - |mlat\_pcb|) \text{ [poleward of the auroral zone]} \end{aligned}$$

Where  $mlat\_azb$  is the magnetic latitude of the auroral zone boundary and  $mlat\_pcb$  is the magnetic latitude of the poleward auroral zone boundary.

The variation of the  $L$  value over a half-orbit goes like this:  $L$  is large ( $\sim 1$ ) at the equator, and decreases to 0 as the spacecraft ascends to the equatorward auroral boundary. In the auroral zone, the boundary is 0 at the equatorward edge and increases to 1 at the poleward edge of the auroral zone. When the spacecraft crosses the poleward edge the  $L$  value drops again to 0, and increases to  $\sim 1$  as the spacecraft approaches the pole, peaking at it's closest approach to the pole, and then decreasing again as the descending leg begins, reaching 0 at the opposite poleward boundary. The  $L$  value jumps up to around 1 at the poleward edge of the oval, decreases to 0 at the equatorward boundary, and then increases to 1 as the spacecraft descends equatorward.

### 2.1.2 Ephemeris Validation

TBD.

### 2.1.3 Caveats and Known Bugs

While we will attempt to minimize bugs, some will show themselves through community usage. They will be prioritized and dealt with as resources permit.

There no known caveats or bugs to document at this time.

### 2.1.4 Revision History

No revisions to date have been made.

## 2.2 SSJ Precipitating Electrons and Ions

The SSJ instrument is described in Hardy et al., (1984) and Schumaker et al., (1988) while the theoretical basis for computing particle fluxes from counts is described in Hardy et al., (2008) and herein. The primary output products include original counts, estimated background counts (C), differential energy fluxes (je), integrated energy fluxes (JE), characteristic energy (Eavg), uncertainty estimates ( $\sigma$ ) for electrons and ions and the spacecraft ephemeris in multiple frames. The uncertainty measures are estimates and covariances have been assumed to be negligible. Where comparable, the equations for uncertainty developed below are agreeable to Bevington and Robinson (1992). In the section that follows, we describe the calculations from the observed counts to scientifically usable quantities.

The observed count in the  $i$ -th channel is compressed onboard then telemetered to the ground and this value is denoted as  $O_i$  in this text. The observed counts are also contaminated by penetrating protons and electrons. Since the SSJ instrument lacks a channel dedicated to measuring the penetrating particle flux, processing at NGDC uses a forward-backward variant of the AFRL algorithm to estimate the background. For each observation, we choose the background ( $B_i$ ) to be the largest of the forward and reverse estimates. The corrected count is given by  $C_i = \text{abs}(O_i - B_i)$ . Note that the adjusted count  $C_i$  is forced to be  $\geq 0$  to be consistent with historical uses and other techniques (e.g. JHU/APL's version of the DMSP adjusted fluxes). A version which allows the adjusted count to float about 0 is available on request. Since original counts ( $O_i$ ) are provided in the public data set, the end user is free to develop their own background adjustment as they see fit. While  $O_i$  is integer valued,  $B_i$  and  $C_i$  are real valued. Figure 2.1 (TBD) shows original counts and the result from estimating the penetrating particle background to remove proton contamination in the South Atlantic Anomaly and central plasma sheet caused by electron contamination near the sub-auroral horns of the radiation belts.

It is assumed that the counts  $O_i$  and  $B_i$  are both Poisson distributed and independent. These assumptions are not completely true because: 1)  $O_i$  was compressed before telemetering, 2)  $B_i$  is estimated from  $O_i$  due to a lack of a dedicated background channel, and 3) the adjusted count  $C_i$  is not allowed to be less than 0.

Note that the sum of two independent Poisson random variables is also Poisson (Lehmann, 1986). Considering Poisson counting statistics and telemetry compression the relative 1-sigma uncertainty associated with the measurement of the true count  $C_i$  is:

$$\frac{\sigma_{C_i}}{C_i} = \frac{\sqrt{\sigma_{O_i}^2 + \sigma_{B_i}^2 + \sigma_{\text{Compression}}^2}}{C_i}, \quad \text{Equation 2.1}$$

$\sigma_{O_i}, \sigma_{B_i}$ : Poisson uncertainties,  $\sqrt{O_i}$ , and  $\sqrt{B_i}$

$\sigma_{\text{Compression}(O_i)}$ : Telemetry compression, determined numerically (see function `ssjdata::get_quantization_uncertainty`).

The uncertainty in a count is dominated by Poisson uncertainty (0-100%) and telemetry compression plays only a minor role (0-2%) when the count is less than 3000-4000. Compression dominates the counting error at higher count levels. The interplay is demonstrated in Figure 2.2. Clearly, the relative uncertainty is undefined for a 0 count event, approaching infinity as the count approaches zero, and the standard Poisson distribution is defined for integral mean counts greater than 1. Thus, we set the absolute and relative uncertainties equal to “undefined” (or IEEE NaN) for counts less than 1. Subsequent mathematical operations ignore NaN values.

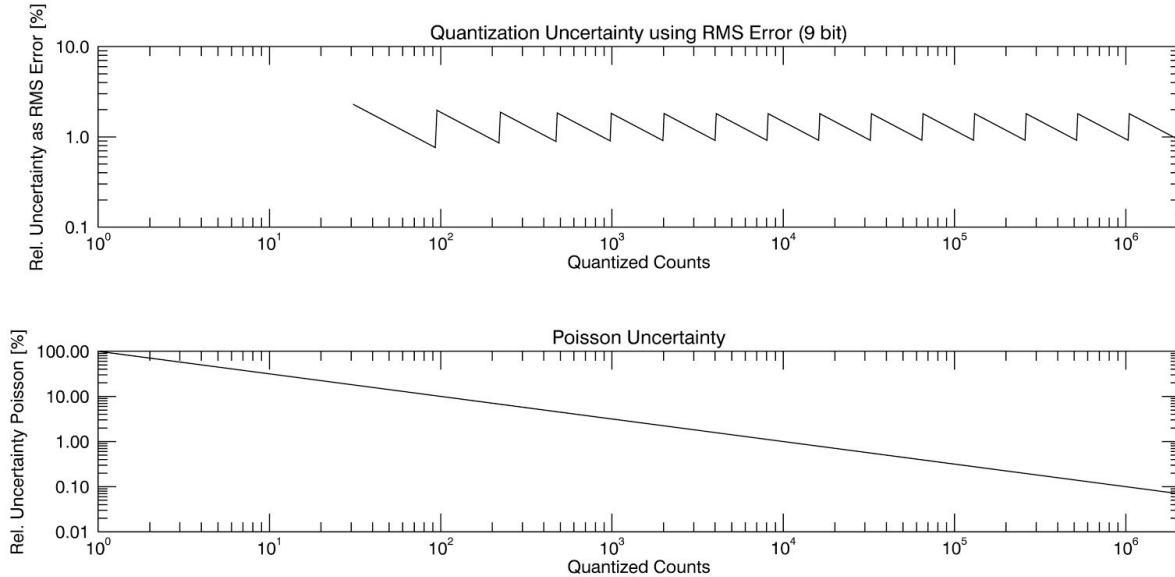


Figure 2.2: Relative uncertainty due to telemetry compression (top) and Poisson counting (bottom) as a function of the count.

Differential electron and ion energy fluxes are calculated from instrument counts. From Hardy et al. (2008) for electrons, we have:

$$j_E(E_i, \Omega) = E_i j_N(E_i, \Omega) = \frac{C_i \cdot E_i}{\eta_{orbit}(E_i) \cdot \eta_{ground}(E_i) \cdot GF_{ground,i} \cdot \Delta t \cdot \Delta E_i} = \frac{C_i \cdot E_i}{GF_i} \quad \text{Equation 2.2}$$

Units :  $\frac{eV}{cm^2 \cdot s \cdot ster \cdot \Delta eV}$

where,

$i$  : channel index, ordered from high to low (30keV down to 30eV)

$E_i$  (eV) : channel central energy for channel  $i$

$\Omega$  : angle

$C_i$  : counts detected for channel  $i$  (contaminated by penetrating particles)

$GF_i$  (cm<sup>2</sup>sr) : effective geometric factor of the sensor (see Eq. 2.3)

$\eta(E_i)$  : efficiency of channel  $i$

$\Delta t$  : dwell time (nominally 0.098 for up through F15 (J4) and 0.05 starting with F16 (J5))

$\Delta E_i$  : effective width (eV) of channel  $i$  (FWHM)

Note that Hardy et al. 2008, uses energy units of keV while we use eV in the current document and the final product files. The channel central energies ( $E_i$ ) are only nominal. The actual channel response functions can be found in [Appendix 7.2](#) (TBD: get from AFRL).

As noted above, the dwell or integration time per energy is nominally 0.098 seconds for SSJ4 (up through F15) and 0.05 seconds for SSJ5 (F16 and greater). The geometric factors ( $GF_{ground,i}$ ) and channel efficiencies  $\eta_{ground}(E_i)$  were determined before launch in the AFRL calibration chamber. As the instrument ages, its degraded efficiency is estimated using methods such as multi-spacecraft intercomparisons and the South Atlantic Anomaly as a standard candle (TBD: ref. Holeman technical memo). Ideally, these four quantities would be separately documented in the final product:  $\eta_{orbit}(E_i)$ ,  $\eta_{ground}(E_i)$ ,  $GF_{ground,i}$ ,  $\Delta t$  and  $\Delta E_i$ . However, the current version of the product files include the lumped quantity for each of electrons and ions as an effective geometric factor:

$$GF_i = \eta_{orbit}(E_i) \cdot \eta_{ground}(E_i) \cdot GF_{ground,i} \cdot \Delta t \cdot \Delta E_i, \quad i \in [1, 19] \quad \text{Equation 2.3}$$

Units :  $cm^2 \cdot ster \cdot sec \cdot \Delta eV$

Assuming the uncertainty in the differential energy flux  $j_E(E_i, \Omega)$  is due predominantly to independent uncertainties in the count ( $C_i$ ) and the effective geometric factor ( $GF_i$ ), the uncertainty can be estimated as follows. This assumes that there is no error in the channel energies; in fact, they are uncertain to a few percent.

Given:

$\sigma_{C_i}$  : Uncertainty in count, includes Poisson, and telemetry compression (see Eq. 2.1).

$\sigma_{GF_i}$  : Uncertainty in effective Geometric Factor. Provided by AFRL.

Then, the relative uncertainty in the differential number and energy fluxes for channel  $i$  is:

$$\frac{\sigma_{j_E(E_i, \Omega)}}{j_E(E_i, \Omega)} = \sqrt{\left(\frac{\sigma_{C_i}}{C_i}\right)^2 + \left(\frac{\sigma_{GF_i}}{GF_i}\right)^2} = \frac{\sigma_{j_N(E_i, \Omega)}}{j_N(E_i, \Omega)} \quad \text{Equation 2.4}$$

Estimated in this manner, the relative uncertainties in differential energy and number flux are identical. Practically, under significant particle flux, the calibration uncertainty (last quantity in the above equation) dominates the effective uncertainty and this quantity has been estimated by AFRL to be approximately 20% for electrons and 50% for ions (Holeman 2014).

The SSJ4 (up to F15) employs a high energy (949eV - 30keV) and a low energy (30eV - 949eV) detector for each of electrons and ions. Since one of the overlapping 949eV channels is sampled at the beginning of the sample period and the other is sampled at the end, their comparison could be used as a measure of the spatial and temporal variability of the aurora over the scan period (e.g. Hardy et al., TBD:REF). The current version of the processing ignores the highest energy of the low energy detector (~ 949 eV). If we choose at a later date to average the overlapping ~ 949 eV channels (10 and 11) as per:

$$j_E(E_{10,11}, \Omega) = \frac{1}{2} \cdot (j_E(E_{10}, \Omega) + j_E(E_{11}, \Omega)) \quad \text{Equation 2.5}$$

then the resultant uncertainty would become:

$$\frac{\sigma_{j_E(E_{10,11}, \Omega)}}{j_E(E_{10,11}, \Omega)} = \frac{1}{2} \cdot \frac{\sqrt{\sigma_{j_E(E_{10}, \Omega)}^2 + \sigma_{j_E(E_{11}, \Omega)}^2}}{j_E(E_{10,11}, \Omega)} \quad \text{Equation 2.6}$$

The total number (energy) flux is calculated in the following manner (adapted from Hardy et al., 2008) by “integrating” differential number (energy) fluxes (Equation 2.2) over energy:

$$\begin{aligned} J_{N, Total}(\Omega) &= j_N(E_1, \Omega) \cdot (E_2 - E_1) + \left[ \sum_{i=2}^{18} j_N(E_i, \Omega) \cdot \frac{(E_{i+1} - E_{i-1})}{2} \right] + j_N(E_{19}, \Omega) \cdot (E_{19} - E_{18}) \\ \text{units} &: \frac{1}{\text{cm}^2 \cdot \text{s} \cdot \text{ster}} \\ J_{E, Total}(\Omega) &= j_E(E_1, \Omega) \cdot (E_2 - E_1) + \left[ \sum_{i=2}^{18} j_E(E_i, \Omega) \cdot \frac{(E_{i+1} - E_{i-1})}{2} \right] + j_E(E_{19}, \Omega) \cdot (E_{19} - E_{18}) \\ \text{units} &: \frac{\text{eV}}{\text{cm}^2 \cdot \text{s} \cdot \text{ster}} \end{aligned} \quad \text{Equation 2.7}$$

The relative uncertainty in the computation of the total number flux  $J_{N, Total}(\Omega)$  and total energy flux  $J_{E, Total}(\Omega)$  can be estimated as follows assuming channels are uncorrelated (i.e. covariance terms are neglected):

$$\frac{\sigma_{J_{N, Total}(\Omega)}}{J_{N, Total}(\Omega)} \approx \sqrt{\sum_{i=1}^{19} (\Delta E_i \cdot \sigma_{j_N(E_i, \Omega)})^2} / J_{N, Total}(\Omega) \quad \text{Equation 2.8}$$

$$\frac{\sigma_{J_{E,Total}(\Omega)}}{J_{E,Total}(\Omega)} \approx \sqrt{\sum_{i=1}^{19} (\Delta E_i \cdot \sigma_{j_E(E_i, \Omega)})^2} / J_{E,Total}(\Omega)$$

where,

$\Delta E_i$  are the energy differences (eV) in Equation 2.7

The relationship between the uncertainty in total number and total energy flux is almost trivial (scaled through the channel central energies  $E_i$  within the summation).

The characteristic energy is calculated as the ratio of the total energy flux and the total number flux (Hardy et al., 2008):

$$E_{Avg} = \frac{J_{E,Total}(\Omega)}{J_{Total}(\Omega)}, \quad \text{units : eV} \quad \text{Equation 2.9}$$

The relative uncertainty in the computation of the average energy can be estimated as:

$$\begin{aligned} \frac{\sigma_{E_{Avg}}}{E_{Avg}} &\approx \sqrt{\left(\frac{\sigma_{J_{E,Total}(\Omega)}}{J_{E,Total}(\Omega)}\right)^2 + \left(\frac{\sigma_{J_{Total}(\Omega)}}{J_{Total}(\Omega)}\right)^2 - 2\left(\frac{\sigma(J_{E,Total} \cdot J_{Total})}{J_{E,Total}(\Omega) \cdot J_{Total}(\Omega)}\right)} \\ \frac{\sigma_{E_{Avg}}}{E_{Avg}} &\leq \sqrt{\left(\frac{\sigma_{J_{E,Total}(\Omega)}}{J_{E,Total}(\Omega)}\right)^2 + \left(\frac{\sigma_{J_{Total}(\Omega)}}{J_{Total}(\Omega)}\right)^2} \quad (\text{approx. upper bound}) \end{aligned} \quad \text{Equation 2.10}$$

While the uncertainties in the energy and number fluxes are not uncorrelated, for simplicity, we use the first two terms as an upper bound for the uncertainty in  $E_{Avg}$ . Numerically, the relative uncertainty in  $E_{Avg}$  is roughly 40% greater than that of the relative uncertainty in the integrated energy flux due to the relative variances in the integrated energy and number fluxes being roughly equal.

Figure 2.3 shows an example auroral crossing for F16 2010-01-10, demonstrating the value of computing useful quantities and providing them in a standard format. For the same time range, Figure 2.4 shows the estimated uncertainties in  $jE$ ,  $JE$ , and  $E_{Avg}$  for electrons (top) and ions (bottom) clearly demonstrating that the uncertainties are smallest under significant auroral signal and increase significantly outside the auroral zone (owing to low count Poisson uncertainty). In the present version, in the auroral zone, differential flux uncertainties are being thresholded under 100% (Figure 2.4 panels 1 and 4). This issue will be looked at in a subsequent version.



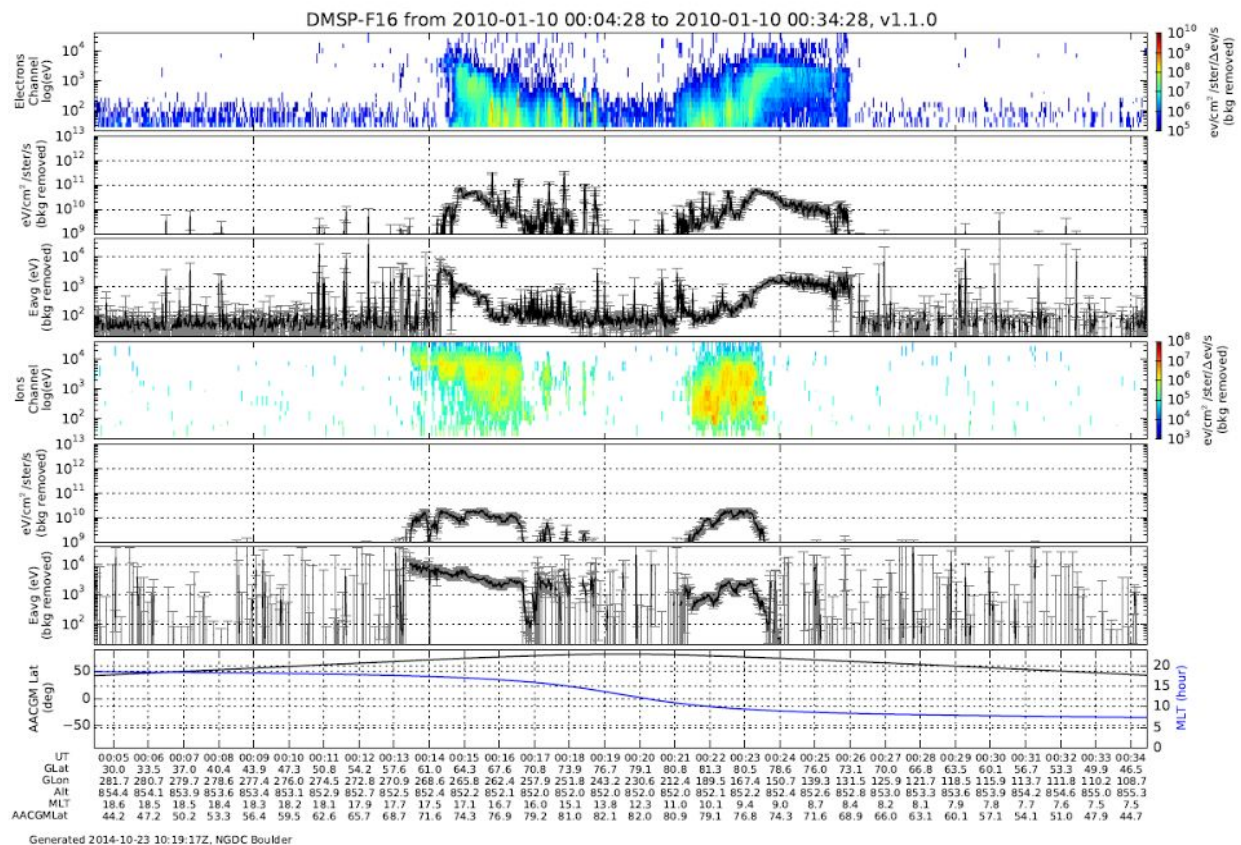


Figure 2.2: F16 2010-01-10 first auroral crossing. Top to bottom: background adjusted electron differential energy flux ( $jE$ ), integrated energy flux ( $JE$ ), average energy ( $E_{avg}$ ); background adjusted ions  $jE$ ,  $JE$ ,  $E_{avg}$ ; AACGM Lat and MLT. Uncertainty bars are shown for the integral quantities but not for the differential quantities.

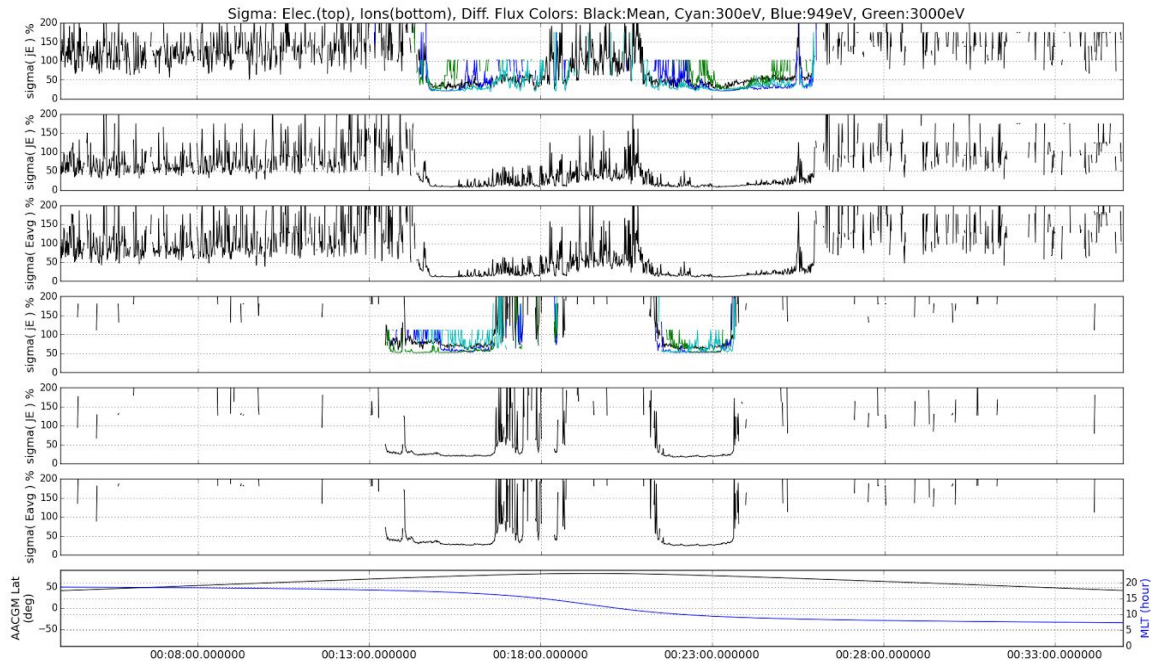


Figure 2.3: Same time range as Figure 2.2. Top to bottom: percent uncertainty in background adjusted electrons JE,  $E_{Avg}$ , percent uncertainty in background adjusted ions JE,  $E_{Avg}$ , AACGM Lat and MLT. TBD: Since  $C_i = O_i - B_i$ , the apparent relative uncertainty thresholding in panels 1 and 4 should be checked.

## 2.2.1 SSJ Validation

TBD

- Plots comparing SSDP, NGDC, JHU/APL
- Table comparing computations using SSDP, NGDC, JHU/APL

## 2.2.2 Caveats and Known Bugs

While we will attempt to minimize bugs, some will show themselves through community usage. They will be prioritized and dealt with as resources permit.

TBD: Add notes from B. Emery.

## 2.2.3 Revision History

TBD.



## 2.3 SSM Magnetic Field and Perturbations

TBD: Are there any QC flags we can add, perhaps based on (temperature, corrections applied, boom versus body mounted,etc)?

The Special Sensor Magnetometer (SSM) was flown as a body mounted fluxgate vector magnetometer on F12 - F14 and as a boom mounted magnetometer on F15 and later spacecraft. From F. Rich ([SSM Geometry.pdf](#), 2001), the SSM sensor's right-handed, orthogonal coordinate frame is defined as:

- +x : positive downward along the local vertical direction
- +y : perpendicular to +x in the forward direction of travel
- +z : perpendicular to +x and +y; toward the night side of the orbit plane

Since the spacecraft's velocity vector is not exactly perpendicular to the local vertical direction at all time, there is a very small angle between the SSM +y direction and the spacecraft's velocity vector.

Both total vector magnetic field (**B**) and vector magnetic perturbations ( $\mathbf{dB} = \mathbf{B} - \mathbf{B}_{IGRF}$ ) are provided. For some spacecraft, the raw data only provided magnetic perturbations. In this case the total field is reconstructed by adding back the appropriate IGRF main field. For spacecraft and days affected, a note is added to the CDF metadata (var: 'B\_SC\_OBS', attr: 'NOTES').

In addition to the original spacecraft frame, the magnetic perturbations are also provided rotated to several other geophysically relevant coordinate systems: geocentric (east,north,up), and magnetic apex (referenced to 110 km altitude, see Richmond, 1995). The Apex 'd' basis set (**d1** - magnetic eastward, **d2** - magnetic equatorward, **d3** - field-aligned) is used.

A unit vector in the direction of the spacecraft's velocity (expressed in geocentric ENU) is also provided. This is an approximation, computed using the geocentric ephemerides and spherical trigonometry (see Appendix XX). No attempt has been made to address the small angle between the spacecraft's velocity vector and the SSM +y direction. It has a very small effect, and is negligible compared to other sources of uncertainty.

### 2.3.1 SSM Validation

The magnetometer aboard the DMSP spacecraft is subject to several noise and uncertainty sources. Previous to F15, the body-mounted magnetometer is strongly affected by signals induced by spacecraft currents. These signals appear as long-period variations in the baseline of the measurements, or as step-up/step-down discontinuities in the baseline. We recommend against using these data in scientific work at this time.

For F15 and later DMSP, the magnetometer was moved to the end of a five meter long boom, in

an attempt to isolate it from spacecraft-induced spurious signals. These data are significantly cleaner, but still suffer from a semi-periodic baseline variation (magnitude of a few hundred nT, period  $\sim$  orbital period), and occasional baseline jump discontinuities (up to 100nT, but usually in the 10s of nT).

For the purposes of analysis of field-aligned current signatures, a simple empirical correction (historically called the MFIT procedure) is used to address the long period baseline. The idea of the process is that field aligned current induced perturbations only appear poleward of the auroral boundary in normal circumstances. This means that any magnetic perturbations observed below polar latitudes are due to one of the several known uncertainty sources (see discussion of measurement uncertainty in next section). Furthermore, most of these sources produce a slowly varying (long spatial frequency) effect on the perturbations, which is roughly oscillatory in nature and is visually very distinct from the perturbations due to currents. By obtaining a smooth polynomial fit to the baseline on either side of the auroral region, one can remove its effect over the auroral region by simply subtracting the polynomial from the perturbation data.

The only assumptions made are that:

1. There is no signal of interest within the slow varying equatorial signal (true unless one is interested in main field anomalies)
2. The baseline can expected not to change abruptly during the transit of the auroral region (true except if there is a turn-on jump discontinuity from something in the spacecraft, which has no net effect on the baseline since the change is reversed when it turns off)

The details of the algorithm follow: for each half-orbit (as determined by crossing the magnetic equator), we use the DMSP midnight equatorward boundary dataset (CEDAR Wiki) and a simple approximation of the auroral oval's eccentricity to estimate the portion of the pass which is below the auroral region, and hence unlikely to contain field-aligned current signatures. Then, for each of the magnetometer axis (X, Y and Z), an odd-order polynomial is fit to the observed perturbations, excluding anything poleward of the boundary. If the root mean squared residual of the fit is less than 20 nT, the polynomial baseline is subtracted from the data and stored as the corrected perturbations. Otherwise, the boundary is moved equatorward five degrees and the process is repeated. If it fails to converge after 3 iterations, the pass is discarded. This procedure effectively removes the long-period baseline oscillations, but not the jump discontinuities.

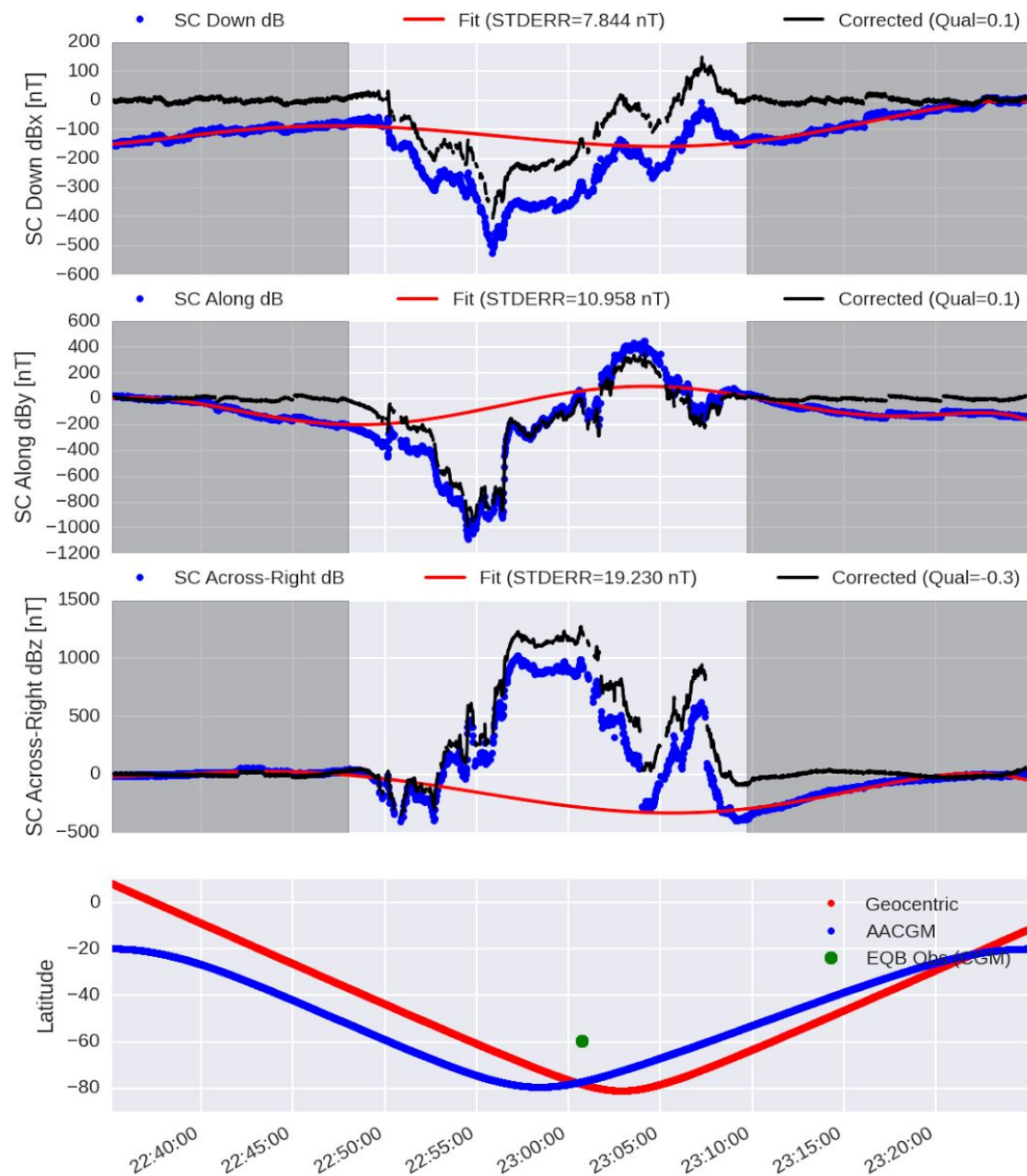


Figure 2.4 - Correcting SSM magnetic perturbations with the MFIT procedure.

Magnetic perturbations (blue) below the auroral oval (shaded) are fit to a polynomial (red) which is subtracted to yield the corrected perturbations (black). The bottom panel shows the latitude of the spacecraft in geocentric and corrected geomagnetic coordinates. The green dot is the latitude and time of the observed equatorward boundary from the midnight EQB database. This polynomial fit did not meet the standard error requirements on first pass, so the fit region has been backed off from the EQB.

### 2.3.2 Uncertainty in the SSM measurements

It is not possible to directly estimate the uncertainty in the SSM magnetic perturbations at this time. In this section we enumerate possible uncertainty sources and show through a comparative study that the uncertainty in the MFIT corrected scalar magnetic perturbations (the magnitude of the perturbation vector) is at most 150 nT (Knipp, 2015).

Although the precision of the detector is documented, and is on the order of a few nanotesla, this does not mean that the measurements are that accurate at representing the field aligned current induced perturbations. The primary problem that comes into any discussion of uncertainty is the presence of unwanted signals that appear in addition to the signal of interest. The following enumerate a few of the sources of uncertainty that can contribute to spacecraft magnetometer observations which use this type of detector:

Uncertainty sources which affect magnetic perturbation *magnitude*, i.e. the scalar perturbation:

1. Model Inaccuracy - The IGRF magnetic field model does not have the resolution in its basis functions to accurately represent many of the magnetic anomalies caused by variations in the composition of the earth's crust.
  - a. Size of effect: ~50 nT on average ( Miller, 2001)
2. Time Shift - The spacecraft can travel some distance over the time between when a measurement is actually acquired by the detector and when it is recorded by the computer. This would mean the IGRF removed at spacecraft location was for a slightly incorrect location. This may differ for different directions, since each core must be sampled sequentially.
  - a. Size of effect: A few nT on average (Miller, 2001)
3. Scalar Offset - The cores of the magnetometer or the surrounding spacecraft can have some remnant magnetization (i.e. they will read some nonzero value when there is no outside field). This is different for each core of the detector, and produces a scalar offset in the baseline.
  - a. Size of effect: up to +-100 nT (Alken, 2014)
4. Spacecraft Currents - The spacecraft's electronics can induce a change in field at the detector (i.e. when the spacecraft uses it's magneto-torquers for attitude control). These show up as a step in one direction in the baseline when they are turned on, and an equal step in the opposite direction when they are turned off.
  - a. Size of effect: up to ~100 nT for short periods, but no net effect (transient)

Uncertainty sources can influence only the perturbation *vector components*, i.e. which magnetometer axis is measuring which portion of the scalar field:

1. Boom Twist (F15 and after) - The 5-meter long booms which hold the magnetometers away from the spacecraft are thought to twist, on the order of tenths of a degree, moving the magnetometer coordinate frame out of alignment with that of the spacecraft.
  - a. Estimated effect: ~.2 degree (Miller, 2001)
2. Non-orthogonality - The cores of the fluxgate magnetometer, which individually measure the X,Y, and Z directions may not be exactly orthogonal to each other due to

manufacturing tolerances.

- a. Estimated effect: up to 0.4 degrees in X-Y, and 0.1 in XZ and YZ (Alken, 2014)
3. Mounting Angle (Before F15) - The body mounted magnetometer may not be mounted exactly aligned with the body-frame.
  - a. Estimated effect: up to .5 degree (Miller, 2001)

**It is important to note that many of these uncertainty sources (scalar offset, nonorthogonality, timeshift, mounting error) have already been addressed in the calibration derived for each spacecraft. This is applied before the data is packaged in the format we begin with for CDF creation, and we have no information about them at this time. We simply enumerate the possible error sources in this type of data for completeness, and to motivate our choice of uncertainty quantification measures.**

The above list gives a rough estimate of the uncertainty in the uncorrected perturbations, however, we have already corrected the data with the MFIT procedure, and, since this process simply applies a correction motivated by geophysics without distinguishing between error sources, we can not create a compound uncertainty of the type used for SSJ. Instead, we have performed a comparative study of the magnetometer observations between DMSP F15 and F16 and NASA's multipoint magnetometer mission ST5 (Knipp, 2015). We found 281 incidences of magnetic conjunction (MC), defined as the DMSP and ST5 orbits intersecting the same IGRF field line at the same time. The time limit for "same-time" was 60 seconds, and the allowable maximum distance the spacecraft could be apart and still be considered in conjunction was 3 degrees great circle distance. The time limit of 60 seconds was chosen because it is the approximate stability time of mesoscale currents on the dayside (Gjelojev, Characteristics of the Field Aligned Current System, TBD add reference).

For the purposes of this uncertainty analysis for DMSP SSM, we will examine a subset of only those MCs which:

1. Occurred in the Northern Hemisphere (where ST5's altitude was similar to DMSP to minimize errors due to 'tracing' along a field line that is potentially open or otherwise deformed from IGRF estimate)
2. Involved one of the trailing ST5 spacecraft (155 or 224), which orbited very close to each other (<120 seconds apart).

Condition 2 will allow us to compare DMSP-ST5 MCs to ST5-ST5 remeasurements very close in time to the MC and give a 'control' to the 'experiment' represented by the magnetic conjunction.

For each MC we compute a magnetic perturbation discrepancy  $|dB_{DMSP} - dB_{ST5}|$  using the as  $dB$  the median magnitude of a group of 1-second observations ( $\sim 20$ ) around the closest approach location for both DMSP and ST5 respectively. The perturbation magnitude is used instead of the vector perturbations for simplicity and to remove the potential effect of the various detector axes misalignment uncertainty sources above. Also we compute a remeasurement perturbation discrepancy  $|dB_{ST5-94} - dB_{ST5-224}|$ , between the ST5 spacecraft involved in the magnetic

conjunction and its partner, which either just measured or will shortly measure the conjunction location.

It turns out that the magnetic perturbation discrepancy between DMSP and ST5 follows a lognormal distribution, as does the remeasurement discrepancy between ST5 224 and ST5 94. We use the remeasurement discrepancy as a proxy for a combination of the ST5 measurement uncertainty and the expected natural variability in the currents during the 60 seconds window for conjunction. Since the difference of two independent lognormal random variables is also lognormal (TBD ref), it follows that the magnetic perturbation discrepancy between DMSP and ST5, minus the associated ST5-ST5 remeasurement discrepancy, also follows the lognormal distribution. We now take this difference as a model for the measurement uncertainty of the DMSP SSM.

Since there are so few samples (only 54 MCs matched the requirements), a meaningful conclusion about the degree of agreement between the two sets of spacecraft can only be arrived at through statistical inference. The variable of interest for the statistical model is the DMSP-ST5 discrepancy adjusted for the natural variability of the system by subtracting the difference in measured magnetic perturbation from the associated ST5-ST5 remeasurement. The lognormal model for this variable is described in figure 4 ( $\mu = 3.331$ ,  $\sigma = 1.327$ ). Figure 4 also shows the histogram from 1000 random draws from the same distribution to demonstrate the feasibility of the model. To put a very conservative upper bound on the DMSP magnetic perturbation uncertainty, one can construct a 99% confidence interval for the mean of this distribution, and find that its upper bound is 142 nT. In other words, if one were to repeat this study on another set of conjunctions an arbitrary number of times one would almost always find the mean adjusted difference to always be less than 150 nT. Since this perturbation discrepancy is also affected by potential inaccuracy in the field line trace and other potential sources of disagreement between the two sets of spacecraft, we can conservatively conclude that the DMSP magnetic perturbation is an accurate representation of the true magnetic perturbation to within 150 nT.

### Figure 2.5: Results of Magnetic Conjunction Study Between DMSP F15 and F16 and ST5

Lines are kernel density estimators for the histograms, representing the implied PDF if the data were normally distributed within each histogram bin. Green represents the distribution of the discrepancy between DMSP and ST5 magnetic perturbations (dB) and blue shows that a lognormal model is reasonable. The 99% confidence upper bound on the mean of the discrepancy is  $\sim 150$  nT, implying that if one were to measure a hypothetical new northern hemisphere conjunction between DMSP and ST5 its value would be less than 150 nT in 99% of such experiments. Thus 150nT uncertainty in the corrected DMSP magnetometer observations is a reasonable conservative upper bound.

#### 2.3.3 Caveats and Known Bugs

While we will attempt to minimize bugs, some will show themselves through community usage. They will be prioritized and dealt with as resources permit.

Body mounted (F13 and before) magnetometer data is contaminated by spacecraft signals.

#### 2.3.4 Revision History

TBD.



## 2.4 SSIES Bulk Plasma Parameters

TBD: Continue discussions with the folks at UTD along the lines of how to best serve the scientific community for time periods where their [DMSP SSIES distribution site](#) provides public data (through 2005).

TBD: Add QC flags (e.g. IDM, RPA).

TBD: Add baseline adjusted perpendicular velocities (nominally  $V_y$ ,  $V_z$ ).

TBD: Error bars?

### 2.4.1 SSIES Validation

TBD.

- Plots and Tables comparing SSDP, NGDC and UTD in 2005 overlap period (from Drew's work).

### 2.4.2 Caveats and Known Bugs

While we will attempt to minimize bugs, some will show themselves through community usage. They will be prioritized and dealt with as resources permit.

### 2.4.3 Revision History

TBD.

## 5 Public Data Access and Tools

Public data access and tools:

- NOAA / NGDC <http://satdat.ngdc.noaa.gov/dmsp/>
- CDAWeb [http://cdaweb.sci.gsfc.nasa.gov/istp\\_public/](http://cdaweb.sci.gsfc.nasa.gov/istp_public/)
- JHU/APL [http://sd-www.jhuapl.edu/Aurora/dataset\\_list.html](http://sd-www.jhuapl.edu/Aurora/dataset_list.html)
- UTD <http://cindispace.utdallas.edu/DMSP/>
- Autoplot
- SPEDAS

## 6 References

TBD: Add:

- DMSP SpWx SSJ SSIES SSM Internal Admin Guide (companion document)
- Coley
- Hardy
- Holeman - in flight SSJ calibration (using the SSA).
- Redmon



- Rich - various tech memos

Alken, P., S. Maus, H. Lühr, R. J. Redmon, F. Rich, B. Bowman, and S. M. O'Malley (2014), Geomagnetic main field modeling with DMSP, *J. Geophys. Res. Space Physics*, 119, 4010–4025, doi:[10.1002/2013JA019754](https://doi.org/10.1002/2013JA019754).

Bevington, P.R., Robinson, D.K. (1992), *Data Reduction And Error Analysis For The Physical Sciences*, McGraw-Hill, ISBN 9780079112439.

Burden, R. L. and Faires, J. D., *Numerical Analysis*, 5th Ed., PWS Publishing Company, Boston, 1993.

Hardy, D. (1984). Precipitating electron and ion detectors (SSJ/4) for the block 5D/flights 6-10 DMSP satellites: Calibration and data presentation. Rep AFGL-TR-84-0317.

Hardy, D. A., Holeman, E. G., Burke, W. J., Gentile, L. C., & Bounar, K. H. (2008). Probability distributions of electron precipitation at high magnetic latitudes. *Journal of Geophysical Research*, 113(A6). doi:10.1029/2007JA012746

Holeman, E. (2014), *Geometric Factor Derivation and Calibration Notes*, AFRL internal technical memo.

Knipp, D. J., T. Matsuo, L. Kilcommons, A. Richmond, B. Anderson, H. Korth, R. Redmon, B. Mero, and N. Parrish (2014), Comparison of magnetic perturbation data from LEO satellite constellations: Statistics of DMSP and AMPERE, *Space Weather*, 12, 2–23, doi:[10.1002/2013SW000987](https://doi.org/10.1002/2013SW000987).

Knipp, DJ, Kilcommons, LM, Gjerloev, J, Redmon, RJ, Slavin, J, and Le, G (2015), A large-scale view of Space Technology 5 magnetometer response to solar wind drivers. *Earth and Space Science*, 2, 115–124. doi: [10.1002/2014EA000057](https://doi.org/10.1002/2014EA000057).

TBD: Kelso REF for celestrak.

Lehmann, E.L. (1986). *Testing Statistical Hypotheses* (second ed.). New York: Springer Verlag. ISBN 0-387-94919-4. page 65.

Miller, N. ; Sexton, L. E. (2001) *Observations and Calibrations of DMSP F15 SSM Data December 1999 - October 2000*. RADEX INC BEDFORD MA, AFRL-VS-TR-2003-1576, Accession Number: ADA419157, <http://www.dtic.mil/cgi-bin/GetTRDoc?Location=U2&doc=GetTRDoc.pdf&AD=ADA419157>

Rich, F.J., (2001) Description of DMSP/SSM data for ionospheric/magnetoaspheric research at [http://satdat.ngdc.noaa.gov/dmsp/docs/SSM\\_Geometry.pdf](http://satdat.ngdc.noaa.gov/dmsp/docs/SSM_Geometry.pdf), accessed on January 13, 2014.

Richmond, A. D. (1995), Ionospheric electrodynamics using Magnetic Apex Coordinates, J. Geomagn. Geoelectr., 47, 191–212.

Redmon, R. J., W. K. Peterson, L. Andersson, E. A. Kihn, W. F. Denig, M. Hairston, and R. Coley (2010), Vertical thermal O<sup>+</sup> flows at 850 km in dynamic auroral boundary coordinates, J. Geophys. Res., 115, A00J08, doi:10.1029/2010JA015589.

Schumaker, T. L. ; Hardy, D. A. ; Moran, S. ; Huber, A. ; McGarity, J. (1988), Precipitating Ion and Electron Detectors (SSJ/4) for the Block 5D/Flight 8 DMSP (Defense Meteorological Satellite Program) Satellite, Air Force Geophysics Lab Hanscom AFB, AFGL-TR-88-0030, Accession Number: ADA203999, 61 pp., <http://www.dtic.mil/get-tr-doc/pdf?AD=ADA203999>.

TBD: Vallado REF from Space Weather paper.

## **7 Appendices**

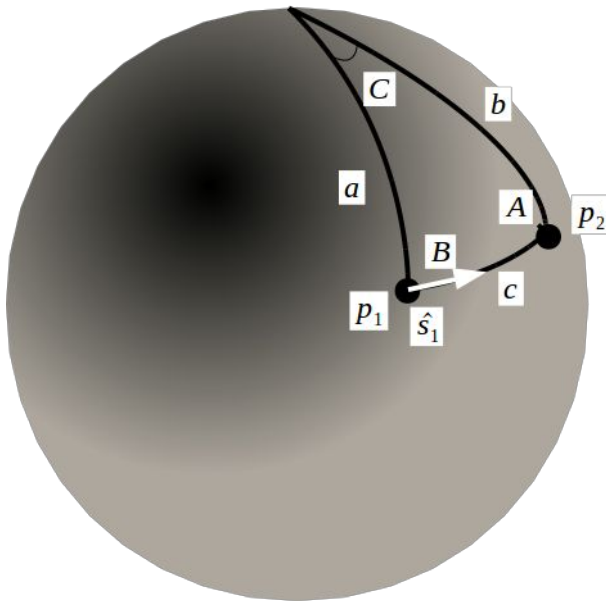
### **7.1 Ephemeris**

TBD: add ECI 1-minute to 1-second interpolation information.

### **7.2 SSJ Detector Efficiencies**

TBD, get from AFRL.

### **7.3 Velocity Direction Approximation**



Given two locations at constant altitude in geocentric spherical coordinates (with lambda as latitude and phi as longitude):

$$p1 = (\lambda_1, \phi_1), p2 = (\lambda_2, \phi_2) \quad \text{eq 7.3.1}$$

Create a spherical triangle where C is the difference in longitudes:  $\phi_2 - \phi_1$  and A and B are the angles between the spherical arc between p1 and p2 and the arcs between p1 and the pole, and p2 and the pole, respectively. Then by applying the law of cosines and the law of sines:

$$\cos(c) = \cos(a)\cos(b) + \sin(a)\sin(b)\cos(C) \quad \text{eq 7.3.2}$$

$$\sin(A) = \sin(a)\sin(C)/\sin(c) \quad \text{eq 7.3.3}$$

$$\cos(A) = \cos(a)\sin(b) - \sin(a)\cos(b)\cos(C)/\sin(c) \quad \text{eq 7.3.4}$$

Note that  $a = 90 - \lambda_1$  is  $a$ ,  $b = 90 - \lambda_2$  and  $C = \phi_2 - \phi_1$

Then if  $s_1$  is a unit vector tangent to the arc between p1 and p2, then its components in geocentric east, north, and up are:

$$s1 = [\sin(A), \cos(A), 0] \quad \text{eq 7.3.5}$$

This algorithm was applied to each pair of adjacent 1-second cadence DMSP locations to obtain a vector which represents the spacecraft direction of travel in geocentric ENU. The s1 vector for

the last datapoint of each day is a duplicate of the second-to-last.

## 7.3 Acronyms

TBD: alphabetize these.

Acronym	Expansion
AACGM	Altitude Adjusted Corrected Geo Magnetic
IDL	Interactive Data Language
ECI	Earth Centered Inertial
J2000	Mean equator and equinox of 2000.0
TOD	True of Date: True equator and equinox
SPDF	Space Physics Data Facility
AFRL	Air Force Research Laboratory
NGDC	National Geophysical Data Center
JHU/APL	Johns Hopkins University Applied Physics Laboratory
CDAWeb	Coordinated Data Analysis Web
SSJ	Special Sensor J
SSM	Special Sensor Magnetometer
SSIES	Special Sensor Ions Electrons and Scintillation
DMSP	Defense Meteorological Satellite Program
UTD	University of Texas Dallas
MLT	Magnetic Local Time